

Large-scale Mesoscopic Transport in Nanostructured Graphene

Haijing Zhang,¹ Jianming Lu,¹ Wu Shi,^{1,*} Zhe Wang,¹ Ting Zhang,¹ Mingyuan Sun,¹ Yuan Zheng,¹ Qihong Chen,¹ Ning Wang,¹ Juhn-Jong Lin,³ and Ping Sheng^{1,2,†}

¹*Department of Physics and William Mong Institute of Nano Science and Technology, HKUST, Clear Water Bay, Kowloon, Hong Kong, China*

²*Institute for Advanced Study, Hong Kong University of Science and Technology, Clear Water Bay, Kowloon, Hong Kong, China*

³*Institute of Physics and Department of Electrophysics, National Chiao Tung University, Hsinchu 30010, Taiwan*

(Received 30 July 2012; published 6 February 2013)

Through exponential sample-size scaling of conductance, we demonstrate strong electron localization in three sets of nanostructured antidot graphene samples with localization lengths of 1.1, 2, and 3.4 μm . The large-scale mesoscopic transport is manifest as a parallel conduction channel to 2D variable range hopping, with a Coulomb quasigap around the Fermi level. The opening of the correlation quasigap, observable below 25 K through the temperature dependence of conductance, makes possible the exponential suppression of inelastic electron-electron scatterings and thereby leads to an observed dephasing length of 10 μm .

DOI: 10.1103/PhysRevLett.110.066805

PACS numbers: 73.23.-b, 72.80.Vp, 72.15.Rn

Mesoscopic phenomena [1] are manifestations of electronic phase effects that persist after multiple elastic scatterings. Dephasing length sets the scale above which the classical diffusive behavior is recovered. Owing to the small size of the dephasing length, one-dimensional (1D) strong electron localization was only recently measured in Si-doped GaAs structure [2], carbon nanotube [3], and graphene nanoribbon [4], while in disordered graphene the average size of two-dimensional (2D) localized states has been inferred from hopping conduction parameters [5–8]. Here we show that graphene [9] with a nanostructured antidot (hole) array can display two parallel conduction channels—the hopping conduction at temperatures higher than 25 K, and the low temperature mesoscopic conduction that exhibits 2D strong localization with a localization length of 1.1, 2, and 3.4 μm in the three sample sets. In the latter there is an exponential scaling of the conductance [10,11] with sample size that extends to 10 μm . The magnetic field dependence of the localization length is in excellent agreement with the theoretical prediction [12].

Classical diffusive transport dictates that in two dimensions, electrical resistance is independent of the sample size as long as it is square in shape. In pristine graphene, ballistic to diffusive transition has been detected at the scale from 500 nm down to 50 nm [13]. Thus for scales larger than one micron, sample size variation serves as a direct and distinguishable approach to detect deviations from the diffusive behavior. Mesoscopic transport provides such a possibility [14].

We have fabricated two types of nanostructured antidot graphene samples [15–18] with different geometry. Sample set A comprises identically nanostructured graphene with the square geometry [shown in inset, Fig. 1(a)], whose sides are 1, 2, 4, 6, 8, and 10 μm . Arranged in a periodic

triangular lattice, the diameter of each antidot is 100 nm and the periodicity is 150 nm. Samples in set B, B1 and B2, are in the Hall bar geometry with the same antidot pattern, but with a bit smaller holes (sample B1, 90 nm) or larger holes (sample B2, 120 nm), while the periodicity remains

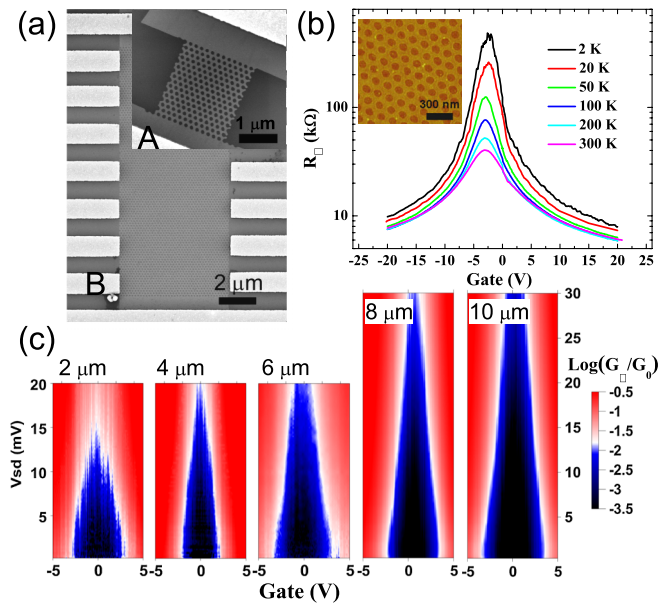


FIG. 1 (color online). (a) SEM images of two sets of nanostructured graphene devices in square geometry (inset), denoted set A, and Hall bar geometry, denoted set B. (b) The sheet resistance of the 2 μm sample from sample set A is plotted as a function of the backgate voltage. Above 20 K, the current used was $I = 50$ nA. The 2 K data were measured at $V_{sd} = 20$ mV. Inset: AFM image of the nanostructured graphene with a periodic triangular lattice of antidots. (c) 2D color maps of conductance shown as a function of the bias voltage, V_{sd} , and the backgate voltage, measured at 2 K. A conductance gap is seen.

150 nm. Samples in set *B* have a length of 14 μm , and the measured conductance is normalized to the sheet conductance (per square) for easy comparison across the three sample sets.

Single layer graphene samples were first prepared by mechanical exfoliation from natural graphite deposited on $\text{SiO}_2(285 \text{ nm})/\text{Si}$ substrate. Metal contacts (10 nm Ti/60 nm Au) were then formed by *e*-beam lithography. The antidot structure was patterned by a second *e*-beam step (Raith eLiNE, 20 kV) followed by oxygen plasma etching. Each sample is contacted by at least four electrodes. The contact resistance is on the order of several hundred Ohms or even smaller. Graphene samples were heated *in situ* to 380 K in high vacuum for several hours to remove the adsorbed impurities.

All measurements were done by using the PPMS (Quantum Design). Electrical measurements were carried out by using a Keithley 2182A nanovoltmeter, a 6221 ac/dc source and an Agilent 4156C semiconductor parameter analyzer. The low temperature data ($T < 20 \text{ K}$) were obtained by applying voltage and measuring the current. In all the magnetotransport measurements, the magnetic field was applied perpendicular to the graphene film.

Figure 1(b) shows a plot of resistance as a function of backgate voltage measured at different temperatures. There is a resistance maximum at $V_g = -2.4 \text{ V}$, denoted the charge neutrality point (CNP). The mobility of the pristine graphene, prior to nanostructuring, can reach 5000–20000 $\text{cm}^2/(\text{V s})$, and the resistance at the CNP is temperature independent down to 2 K. After patterning into antidot geometry, the mobility is lowered to 750 $\text{cm}^2/(\text{V s})$ at room temperature. The resistance increases as the temperature decreases [see Fig. 1(b)] and exhibits a large (gate voltage) on/off ratio at 2 K. The focus of our study, the mesoscopic transport properties, is carried out near the CNP.

All samples exhibit large negative magnetoresistance [$\text{MR} = (R(B) - R(B = 0))/R(B = 0)$] at low temperatures, tunable by the backgate voltage. At CNP, which has the lowest carrier density, the most dramatic negative magnetoresistance—up to 90% at 4 T—was measured at 2 K for the 10 μm sample. This negative MR is similar to those reported in graphene nanoribbons [19]. At a higher carrier density ($V_g - V_{\text{CNP}} = \pm 20 \text{ V}$), the negative MR gradually drops to about 30%. (MR data are shown in Ref. [20].) At 2 K, all samples exhibit a small transport gap near the CNP. We have measured the conductance at different source-drain voltages near the CNP, and plotted in color the 2D maps for different sample sizes as shown in Fig. 1(c). The dark areas are regions of strongly suppressed conductance. We can see that the transport gap broadens with increasing sample size, indicating the potential existence of a nondiffusive, mesoscopic conduction channel at low temperatures.

To clearly visualize the two parallel channels of conduction in our nanostructured graphene, we plot in Fig. 2

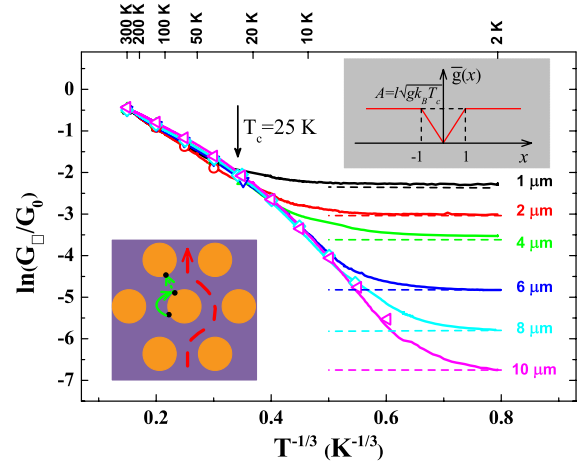


FIG. 2 (color online). Logarithm of the sheet conductance of sample set *A*, in units of G_0 , is plotted as a function of $T^{-1/3}$. The solid lines are measured data while the open symbols are calculated from Eq. (1). The dashed lines are used to highlight the plateau regime. Lower inset: A cartoon picture illustrating the two parallel types of conduction. The upper inset shows the density of states as a function of $x = \epsilon/k_B T_c$ used to account for the temperature dependence of the hopping conduction.

the logarithm of the measured conductance for the six samples of sample set *A* at CNP as a function of $T^{-1/3}$, in anticipation of observing 2D variable range hopping (VRH) conduction [21]. At room temperature (RT), the resistances of the six samples are nearly the same (varying slightly as $39 \pm 3 \text{ k}\Omega$), in accordance with the diffusive transport behavior. To remove the small fluctuations that can arise from the slight differences in sample fabrication, we normalize the conductance data so that all samples have RT resistance of 39 $\text{k}\Omega$. In addition, we express the conductance in units of the quantum conductance $G_0 = e^2/h$.

It can be seen that from 300 to 25 K the normalized conductance of all the samples bundles together and follows a linear relation. This is clearly the 2D VRH regime, defined by $\ln G \propto (T_0/T)^\alpha$ with $\alpha = 1/3$. Below 25 K, however, the temperature dependence of conductance is shown to follow a $\alpha = 1/2$ trajectory (see below) before approaching a flat plateau. Different samples display very different plateau values that can be orders of magnitude apart. Such nondiffusive behavior clearly delineates the mesoscopic conduction channel in parallel to the VRH. In the plateau regime, as indicated by the dashed lines in Fig. 2, conductance follows very well the relation $G = G^l \exp(-L/\xi)$, where L denotes the sample size and ξ is the localization length that characterizes the exponential spatial variation of mesoscopic conductance.

We interpret the transition from $\alpha = 1/3$ to $\alpha = 1/2$ by the opening of a Coulomb quasigap around the Fermi level, shown schematically in the upper inset of Fig. 2. In two dimensions the density of states within the Coulomb quasigap should be linear in energy [22]. The demarcation point between the Coulomb quasigap and the constant

variable range hopping is given by $k_B T_c$ with $T_c = 25$ K. We have developed a model [20] to depict the temperature dependence of conductance in this situation:

$$G = \gamma_0 \exp\left[-\left(\frac{3T_c^{1/3}}{2A^{2/3}}\right)T^{-1/3} - \left(\frac{T_c}{2}\right)T^{-1}\right]; \quad T > T_c$$

$$G = \gamma_0 \exp\left[-\left(2\sqrt{\frac{T_c}{A}}\right)T^{-1/2}\right]. \quad T \leq T_c \quad (1)$$

The symbols shown in Fig. 2 represent the predictions of Eq. (1) with the dimensionless constant $A = 0.58$ and $\gamma_0 = 1.77G_0$. Excellent agreement is seen. The opening of the Coulomb quasigap not only gives a good account of the temperature dependence of conductance, but also offers consistent estimates of the various length and energy scales [20]. But perhaps the most important is that the Coulomb quasigap enables the observation of the large-scale mesoscopic conductance, through the suppression of the inelastic electron-electron scattering. This exponential suppression of the inelastic scattering was theoretically predicted over a decade ago [23] but has rarely been experimentally tested [24]. This point will be further elaborated below.

There can be a simple correspondence between the sample nanostructure and the two types of conduction channels. We ascribe the localized states responsible for the high temperature (i.e., >25 K) hopping conduction to be associated with the edges created by the antidot array [25,26], with elastic scatterings within the domain of a single hole. Electrical conduction occurs when such a localized electron hops (with thermal excitation) to a neighboring hole (lower inset to Fig. 2, where the green arrow indicates an elastic scattering and the dotted line is meant to denote a hop to a neighboring hole's edge state).

For the VRH channel, a hopping distance between such localized states can be estimated by using the equation [27]: $\xi_{\text{VRH}} = \sqrt{13.8/[k_B g_{\text{VRH}} T_0]}$, where k_B is the Boltzmann constant, T_0 being the slope in the high temperature limit (Fig. 2), and $g_{\text{VRH}} = 8 \times 10^{16}/(\text{eV m}^2)$ is the density of states that can be obtained from the Einstein relation. Here we have used the measured conductance at room temperature. This value for the density of states is close to those reported in Refs. [6–8,28]. With the above value of g_{VRH} , we obtain $\xi_{\text{VRH}} = 50$ nm (± 5 nm), which is just the constriction width between two neighboring holes and therefore consistent with our physical picture.

The low temperature transport (i.e., <25 K) is attributed to the localized electrons in the nanoribbon network, away from the edges of the holes (illustrated by the red dashed line and arrow in the lower inset to Fig. 2). They should have a larger localization length, since the region of (wave function) support is relatively intact. Owing to the Coulomb quasigap, they exhibit a different temperature dependence, $\ell n G \propto T^{-1/2}$. For a finite-sized sample, however, the low temperature conductance would be dominated by the state,

at or very close to the Fermi level, that has the largest localization length. This represents the parallel channel of (temperature-independent) mesoscopic conductance.

According to the scaling theory of localization [11], in 2D disordered systems increasing sample size renormalizes the diffusion constant downward (starting from the Boltzmann diffusion constant $D_B = v_F^2 \tau / 2$), via the mechanism of coherent backscattering. When the dephasing length $l_\varphi > L$, the 2D conductance decreases exponentially with L . This is the strong localization regime as predicted by theory [10,29].

In Fig. 3(a) we plot the logarithm of the 2 K conductance data of sample B1, measured at the CNP (black circles), as a function of L . Below $L = 10$ μm , an excellent linear relation is obtained, just as predicted from simulations [29]. The red solid straight line is a linear fit to the conductance data for sample sizes smaller than 10 μm , which indicates a localization length $\xi_0 = 3.4$ μm ($\xi_0 = 1.12$ μm for B2; data shown in Ref. [20]). However, when L exceeds 10 μm , the conductance per square obeys the Ohmic behavior and becomes independent of L . Such a crossover from the non-diffusive to the diffusive regime in a single sample is a clear indication that the dephasing length is in fact just 10 μm .

Also shown in Fig. 3(a) is that away from the CNP, e.g., $V_g - V_{\text{CNP}} = 12$ V, the conductance of all samples is larger than the quantum conductance (shown within the grey region), and the system has made the transition to the weak localization regime [30,31], with no size scaling effect. Simultaneously, the $\alpha = 1/2$ behavior is also absent in the low temperature behavior of the hopping conduction.

In Fig. 3(b) the size dependence of the conductance from samples in set A is shown for different applied magnetic

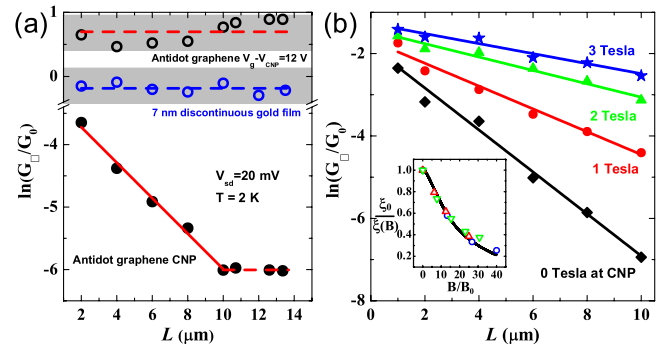


FIG. 3 (color online). (a) Conductance G_{\square} of sample B1 is plotted as a function of sample size L . Black open circles are for gate voltage $V_g - V_{\text{CNP}} = 12$ V and blue open circles are for a 7 nm discontinuous gold film as a reference sample. Here G_{\square} was measured at 2 K with $V_{\text{sd}} = 20$ mV. The red solid line is a linear fit to the data. The dashed lines are guides to the eyes. (b) Conductance G_{\square} from sample set A is plotted as a function of sample size L at different magnetic field. Inset: $1/\xi(B)$ is plotted as a function of the magnetic field, normalized by B_0 . Here, ξ_0 is the zero field value. The black line is the theory prediction [12], the blue symbols are for samples in set A, and red and green symbols are for samples B1 and B2, respectively.

fields up to 3 T. From the 0 T slope we deduce the localization length ξ_0 to be 2 μm . Such a large 2D localization length has been theoretically predicted [32–34], with a relation to the elastic mean free path l_m as $\xi \cong l_m \exp[(\pi/2)k_F l_m]$ [14], in which k_F denotes the Fermi wave vector. By estimating $k_F = \sqrt{n\pi}$, where the carrier density $n = 2.5 \times 10^{11} \text{ cm}^{-2}$ at the CNP may be obtained by fitting the RT conductance $G^{-1} = G_s^{-1} + (ne\mu)^{-1}$ [20,35], we obtain $l_m = 30 \text{ nm}$ ($l_m = 33, 26 \text{ nm}$ for samples *B1* and *B2*, respectively). Here the fitted G_s^{-1} for our samples ranges from 1–3 k Ω . It has a minimal effect on the value of the carrier density.

It is seen clearly in Fig. 3(b) that the localization length increases with an applied magnetic field. The precise behavior has been predicted by Ono [12] for 2D strong Anderson localization. In the inset to Fig. 3(b) we fit all three data sets to the theory prediction. Excellent agreement is obtained. Separately, the magnetic field dependence of ξ_{VRH} is shown in Ref. [20].

From Fig. 3(b) inset and Ref. [12], we have $B/B_0 = (ev_F^2\tau^2/\hbar)e^{1/\lambda}B$, in which B_0 is a function of the elastic scattering time τ , and $\lambda = \hbar/E_F\tau$ is a dimensionless coupling constant. This relation between B_0 and τ offers an alternative approach to estimate the elastic mean free path. Since B_0 is 0.075 T from our data of sample set *A* ($B_0 = 0.04, 0.13 \text{ T}$ for *B1* and *B2*, respectively), we obtain an estimate of $\tau = 28 \text{ fs}$. The Boltzmann diffusion constant is therefore $D_B = v_F^2\tau/2 = 1.4 \times 10^{-2} \text{ m}^2/\text{s}$, and the mean free path is $l_m = v_F\tau = 28 \text{ nm}$ ($l_m = 32, 24 \text{ nm}$ for *B1* and *B2*, respectively). This value is noted to be consistent with the $l_m = 30 \text{ nm}$ (33 and 26 nm for *B1* and *B2*) deduced earlier. The density of states can also be deduced, based on the relation $g = G/e^2D_B$. Here the conductance is that of the 1 μm sample measured at 2 K, so that $g = G/e^2D_B = 1.7 \times 10^{15}/(\text{eV m}^2)$. Thus the states with larger localization lengths have $\sim 1/50$ the DOS responsible for the VRH. Our model, Eq. (1), is based on the simplified picture of two DOS groupings and the resulting temperature variation in conductance.

The low density of states, coupled with the Coulomb quasigap, constitute the very reason for the very large dephasing length that makes our observations possible. For an Anderson-localized state at the Fermi level, if there is a finite electronic level separation $\Delta\varepsilon$ to the next excited state, then the electron-electron scattering can not cause dephasing at those temperatures $T \ll \Delta\varepsilon/k_B$. Here the spatially averaged value of the gap is on the order of $k_B T_c$; hence for $T \ll 25 \text{ K}$, inelastic electron-electron scatterings will be exponentially suppressed [23]. The low density of states at low temperatures is also explained by the Coulomb quasigap, which depletes the density of states close to the Fermi level. The 1.1–3.4 μm Anderson-localized state, as it is manifest only at low temperatures, should be at, or very close to, the Fermi level.

One can also measure the dephasing length from the Aharonov-Bohm (AB) effect [18]. Associated with the AB effect data there is always an effective radius r of the circular current path around the holes, with a path length $\pi r \sim 200 \text{ nm}$. We attribute the dephasing length measured by the AB effect to be associated with the tightly localized edge states, which are much more numerous than the states at the Fermi level. Since the edge states can inevitably induce spin-flip scatterings, hence the dephasing lengths obtained from the AB effect are expected to be much smaller [18]. In this context the size scaling approach, over the 1 to 10 micron range, provides a rather unique method to access the large dephasing length associated with the states at the Fermi level. However, related issues deserve to be further investigated.

It may be puzzling at first sight to observe a significantly larger dephasing length in a nanostructured graphene sample than in pristine graphene [31]. However, whereas pristine graphene is a poor metal, here the Fermi level state is Anderson localized with a Coulomb quasigap. A qualitatively similar situation was encountered in disordered indium oxide [24], in which a significantly smaller inelastic electron-electron scattering rate, as compared to the crystalline case, has been attributed to the discreteness of the local energy spectrum at the Fermi level.

In graphene, electron-phonon interaction is weak, especially at low temperatures [36–38]. A detailed study of the dephasing length in graphene and the condition for achieving a large value would not only be scientifically interesting, but also important technologically.

P. S. wishes to thank Tian Chushun for the suggestion of a reference. This work was supported by the SRFI11/SC02 and the Research Grants Council of Hong Kong Grant No. HKUST9/CRF/08. Technical support of the Raith-HKUST Nanotechnology Laboratory for the *e*-beam lithography facility at MCPF (Project No. SEG_HKUST08) is hereby acknowledged. J. J. L was supported by the Taiwan National Science Council through Grant No. NSC 101-2120-M-009-005.

*Present address: Department of Applied Physics, University of Tokyo, Tokyo, Japan.

†Corresponding author.
sheng@ust.hk

- [1] P. A. Lee and T. V. Ramakrishnan, *Rev. Mod. Phys.* **57**, 287 (1985).
- [2] M. E. Gershenson, Y. B. Khavin, A. G. Mikhalechuk, H. M. Bozler, and A. L. Bogdanov, *Phys. Rev. Lett.* **79**, 725 (1997).
- [3] C. Gomez-Navarro, P. J. D. Pablo, J. Gomez-Herrero, B. Biel, F. J. Garcia-Vidal, A. Rubio, and F. Flores, *Nat. Mater.* **4**, 534 (2005).
- [4] G. Xu, C. M. Torres, J. Tang, J. Bai, E. B. Song, Y. Huang, X. Duan, Y. Zhang, and K. L. Wang, *Nano Lett.* **11**, 1082 (2011).

- [5] D. C. Elias, R. R. Nair, T. M. G. Mohiuddin, S. V. Morozov, P. Blake, M. P. Halsall, A. C. Ferrari, D. W. Boukhvalov, M. I. Katsnelson, A. K. Geim, and K. S. Novoselov, *Science* **323**, 610 (2009).
- [6] X. Hong, S. H. Cheng, C. Herding, and J. Zhu, *Phys. Rev. B* **83**, 085410 (2011).
- [7] J. Moser, H. Tao, S. Roche, F. Alzina, C. M. S. Torres, and A. Bachtold, *Phys. Rev. B* **81**, 205445 (2010).
- [8] W. Li, Y. He, L. Wang, G. Ding, Z.-Q. Zhang, R. W. Lortz, P. Sheng, and N. Wang, *Phys. Rev. B* **84**, 045431 (2011).
- [9] A. K. Geim and K. S. Novoselov, *Nat. Mater.* **6**, 183 (2007).
- [10] P. W. Anderson, *Phys. Rev.* **109**, 1492 (1958).
- [11] E. Abrahams, P. W. Anderson, D. C. Licciardello, and T. V. Ramakrishnan, *Phys. Rev. Lett.* **42**, 673 (1979).
- [12] Y. Ono, *Prog. Theor. Phys. Suppl.* **84**, 138 (1985).
- [13] Y. Wu, V. Perebeinos, Y.-m. Lin, T. Low, F. Xia, and P. Avouris, *Nano Lett.* **12**, 1417 (2012).
- [14] P. Sheng, *Introduction to Wave Scattering, Localization, and Mesoscopic Phenomena* (Springer, New York, 2006), 2nd ed.
- [15] J. Bai, X. Zhong, S. Jiang, Y. Huang, and X. Duan, *Nat. Nanotechnol.* **5**, 190 (2010).
- [16] T. Shen, Y. Q. Wu, M. A. Capano, L. P. Rokhinson, L. W. Engel, and P. D. Ye, *Appl. Phys. Lett.* **93**, 122102 (2008).
- [17] J. Eroms and D. Weiss, *New J. Phys.* **11**, 095021 (2009).
- [18] A. J. M. Giesbers, E. C. Peters, M. Burghard, and K. Kern, *Phys. Rev. B* **86**, 045445 (2012).
- [19] J. Bai, R. Cheng, F. Xiu, L. Liao, M. Wang, A. Shailos, K. L. Wang, Y. Huang, and X. Duan, *Nat. Nanotechnol.* **5**, 655 (2010).
- [20] See Supplemental Material at <http://link.aps.org/supplemental/10.1103/PhysRevLett.110.066805> for (i) magnetoresistance at different gate voltages measured at 2 K; (ii) a derivation of the temperature dependence of conductance with a Coulomb gap; (iii) determination of residual charge carrier density n_0 ; (iv) bias voltage dependence; (v) additional experimental data on different antidot size and spacing; and (vi) magnetic field dependence of ξ_{VRH} .
- [21] N. F. Mott, *J. Non-Cryst. Solids* **8–10**, 1 (1972).
- [22] B. I. Shklovskii and A. L. Efros, *Electronic Properties of Doped Semiconductors* (Springer-Verlag, Berlin, 1984).
- [23] Y. M. Blanter, *Phys. Rev. B* **54**, 12807 (1996).
- [24] Z. Ovadyahu, *Phys. Rev. Lett.* **108**, 156602 (2012).
- [25] M. Y. Han, B. Özyilmaz, Y. Zhang, and P. Kim, *Phys. Rev. Lett.* **98**, 206805 (2007).
- [26] C. Stampfer, J. Güttinger, S. Hellmüller, F. Molitor, K. Ensslin, and T. Ihn, *Phys. Rev. Lett.* **102**, 056403 (2009).
- [27] A. S. Skal and B. I. Shklovskii, *Sov. Phys. Solid State* **16**, 1190 (1974).
- [28] F. Withers, M. Dubois, and A. K. Savchenko, *Phys. Rev. B* **82**, 073403 (2010).
- [29] P. Sheng, *Philos. Mag.* **B 65**, 357 (1992).
- [30] E. McCann, K. Kechedzhi, V. I. Fal'ko, H. Suzuura, T. Ando, and B. L. Altshuler, *Phys. Rev. Lett.* **97**, 146805 (2006).
- [31] F. V. Tikhonenko, D. W. Horsell, R. V. Gorbachev, and A. K. Savchenko, *Phys. Rev. Lett.* **100**, 056802 (2008).
- [32] A. Lherbier, B. Biel, Y.-M. Niquet, and S. Roche, *Phys. Rev. Lett.* **100**, 036803 (2008).
- [33] A. Lherbier, X. Blase, Y.-M. Niquet, F. Triozon, and S. Roche, *Phys. Rev. Lett.* **101**, 036808 (2008).
- [34] N. Leconte, A. Lherbier, F. Varchon, P. Ordejon, S. Roche, and J. C. Charlier, *Phys. Rev. B* **84**, 235420 (2011).
- [35] C. Jang, S. Adam, J. H. Chen, E. D. Williams, S. D. Sarma, and M. S. Fuhrer, *Phys. Rev. Lett.* **101**, 146805 (2008).
- [36] J. J. Lin, *Physica (Amsterdam)* **B279**, 191 (2000).
- [37] J. J. Lin and J. P. Bird, *J. Phys. Condens. Matter* **14**, R501 (2002).
- [38] T. Stauber, N. M. R. Peres, and F. Guinea, *Phys. Rev. B* **76**, 205423 (2007).

Supplementary Material

for

“Large Scale Mesoscopic Transport in Nanostructured Graphene”

I. Magnetoresistance at different gate voltages measured at 2K

Figure S1 shows the magnetoresistance ($MR = (R(B) - R(B=0)) / R(B=0)$) measured at 2 K for different gate voltages. The resistance has been normalized by the resistance measured at 0 Tesla. It is seen in Fig. S1 that the negative magnetoresistance is the largest at the charge neutrality point (CNP), reaching -90% at 4 Tesla. As the gate voltage deviates from the CNP, the negative magnetoresistance gradually drop to -30% at 4 Tesla.

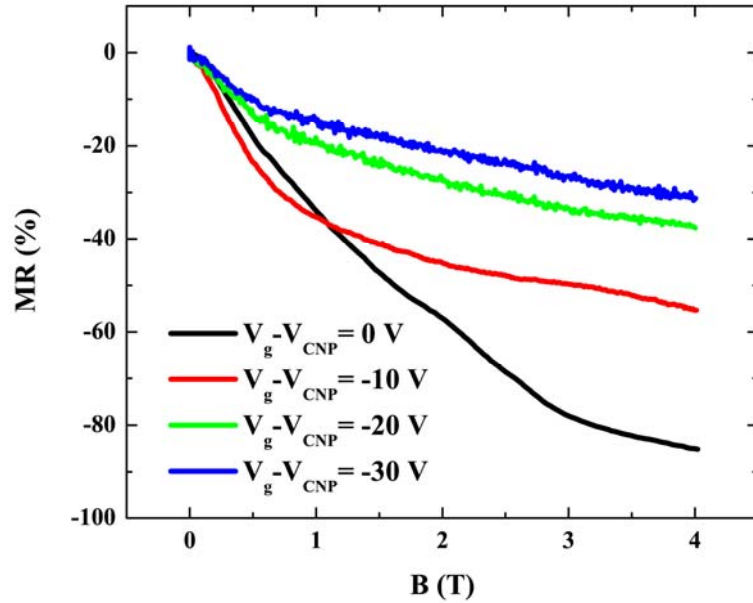


FIG. S1. Magnetoresistance of the $L=6 \mu\text{m}$ antidot graphene sample measured at 2K, for different gate voltages. The bias current used was $I_{sd} = 5 \text{ nA}$.

II. Temperature dependence of conductance with a Coulomb gap

2A. Derivation of the hopping conduction expression

We start from the following equation in deducing the VRH behavior [1]:

$$G \propto \exp \left[- \left(\frac{1}{N^{1/2}(\varepsilon)l} + \frac{\varepsilon}{k_B T} \right) \right],$$

where $N(\varepsilon)$ is the carrier density in units of 1/Area; l characterizes the size of the localized states. $N(\varepsilon)$ is the energy integral of g , where g is the density of states. The temperature dependence of 2D hopping conductance, $G \sim \exp[-(T_o/T)^{-\alpha}]$ with $\alpha = 1/3$, is derived with the assumption of constant density of states. Suppose a Coulomb quasigap is opened in the density of states g around the Fermi level. In 2D such a quasigap is linear in ε , measured relative to the Fermi level. For the purpose of deriving the temperature dependence of hopping conductance, let us start from the dimensionless $\bar{g} = g / \sqrt{g/l^2 k_B T_c}$. Here g and l can take either of the two values—for the states close to the Fermi level (the Coulomb quasigap) or for those further away from the Fermi level (those responsible for the high temperature 2D hopping). In Fig. S2 we show \bar{g} plotted as a function of $x = \varepsilon / k_B T_c$. This simple model may be expressed as

$$\bar{g}(x) = A |x|; \quad |x| \leq 1,$$

$$\bar{g}(x) = A; \quad |x| > 1.$$

Here $A = l \sqrt{g k_B T_c}$. The advantage of this formulation is that while A is an approximate constant, the size of the localized state l can vary independently, with the condition that $l \sqrt{g}$ must remain invariant (so that A remains a constant). This criterion is based on the fact that the average separation \bar{r}_{ij} between the localized states selects the participating states to be those with the comparable sizes. This is because $l \gg \bar{r}_{ij}$ would imply

thermal activation behavior instead of hopping. In the other limit of $l \ll \bar{r}_{ij}$, the contribution to the overall hopping conductance would be minimal. Hence we should have $l \sim \bar{r}_{ij}$. Constancy of $l\sqrt{g}$ follows because $g \sim \bar{r}_{ij}^{-2}$. In our case we shall have a low temperature regime and a high temperature regime, with different values of l and g in the two regimes. The constancy of A then serves as a consistency check for the model against the experimental data.

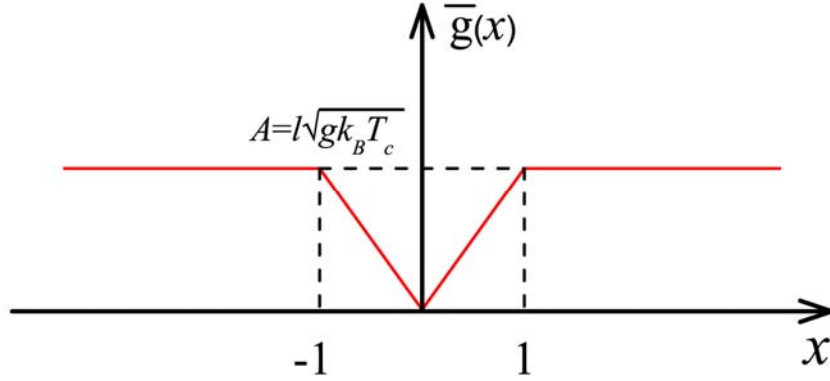


FIG. S2. Dimensionless density of states as a function of $x = \varepsilon / k_B T_c$.

It follows that

$$\begin{aligned} \bar{N}(x) &= \int_{-1}^1 \bar{g}(x) dx = Ax^2; & |x| \leq 1 \\ \bar{N}(x) &= 2 \int_1^x \bar{g}(x) dx + A = A(2|x| - 1); & |x| > 1 \end{aligned}$$

Then the hopping conduction probability has the form

$$\exp\left[-\left(\frac{1}{\ell\sqrt{N(\varepsilon_0)}} + \frac{\varepsilon_0}{kT}\right)\right] = \exp\left[-\left(\frac{1}{\sqrt{A\bar{N}(x)}} + \frac{xT_c}{T}\right)\right]. \quad (\text{S1})$$

Maximizing the hopping conduction probability with respect to x yields

$$x_m = \sqrt{\frac{T}{AT_c}}; \quad |x| \leq 1$$

$$x_m = \frac{1}{2} \left(\frac{T}{AT_c} \right)^{2/3} + \frac{1}{2}; \quad |x| > 1$$

Substituting the above into Eq. (S1), we have for the low temperature regime

$$G \propto \exp \left[- \left(2 \sqrt{\frac{T_c}{A}} \right) T^{-1/2} \right]$$

and

$$G \propto \exp \left[- \left(\frac{3T_c^{1/3}}{2A^{2/3}} \right) T^{-1/3} - \left(\frac{T_c}{2} \right) T^{-1} \right]$$

for the high temperature regime. As the influence of $1/T$ term is small, the predominant behavior is still $T^{-1/3}$ at high temperatures. Hence in the high temperature regime the behavior is still that of 2D variable range hopping.

2B. Consistency checks of the Coulomb gap model against experimental parameters

We use the value of g deduced experimentally to check the consistency of the Coulomb gap model. Since the total number of localized states within the quasigap is given by $N = gk_B T_c = 1 / (\pi r_{ij}^2)$, the average separation between these localized states can be estimated to be $r_{ij} = 300$ nm. With $l = r_{ij} = 300$ nm and $g = 1.7 \times 10^{15} / (\text{eV} \cdot \text{m}^2)$, we get the dimensionless constant $A = 0.574$, which is precisely the value obtained from fitting the data by using Eq. (1) in the main text. For the regime of $T > T_c$, if we use the DOS calculated from Mott VRH $g_{VRH} = 8 \times 10^{16} / (\text{eV} \cdot \text{m}^2)$ and the same value of A , then the value $l = \xi_{VRH} = 43.5$ nm is obtained, which is in reasonable agreement with $\xi_{VRH} = 50$ nm obtained previously. Moreover, since $e^2 / 4\pi\kappa\epsilon_0 r_{ij}$ with $\kappa = 2.45$ [3] yields a Coulomb gap $\Delta\epsilon$, we can use $r_{ij} = 300$ nm to obtain $\Delta\epsilon = 1.96$ meV, corresponding to a temperature

of 23 K. This value is very close to the observed $T_c = 25$ K. The above consistency checks further confirm the existence of a Coulomb quasigap in our samples.

It might be argued that the states far away from the Fermi level may also exhibit the correlation effect. However, such effect, against a high density of states background, can hardly be distinguished from the $\alpha = 1/3$ to $1/2$ crossover delineated by our simplified model.

III. Determination of residual charge carrier density n_0

We fit the conductivity data to

$$G^{-1} = G_s^{-1} + (ne\mu)^{-1} \quad , \quad (\text{S2})$$

where G_s comes from short-range scattering and is independent of the carrier density, n is the total carrier density. $n = \sqrt{n_0^2 + n_*^2}$, where n_0 is the residual charge carrier density induced by electron-hole puddle and n_* is the carrier density that can be tuned by the back gate voltage [2]. $n_* = c_g |V_g - V_{CNP}| / e$, e is the elementary electric charge and $c_g = 1.2 \times 10^{-8} \text{ F / cm}^2$ is the back gate capacitance per unit area for the 285 nm thick SiO_2 .

We use the resistance data shown in Fig. 1(b), measured at 300 K, for our analysis. Shown below in Fig. S3 is the experimentally measured resistance as a function of gate voltage (black solid line), and the fitting based on Eq. S(2) (red solid circles). From the fitting, the residual carrier density $n_0 = 2.5 \times 10^{11} \text{ cm}^{-2}$ is obtained.

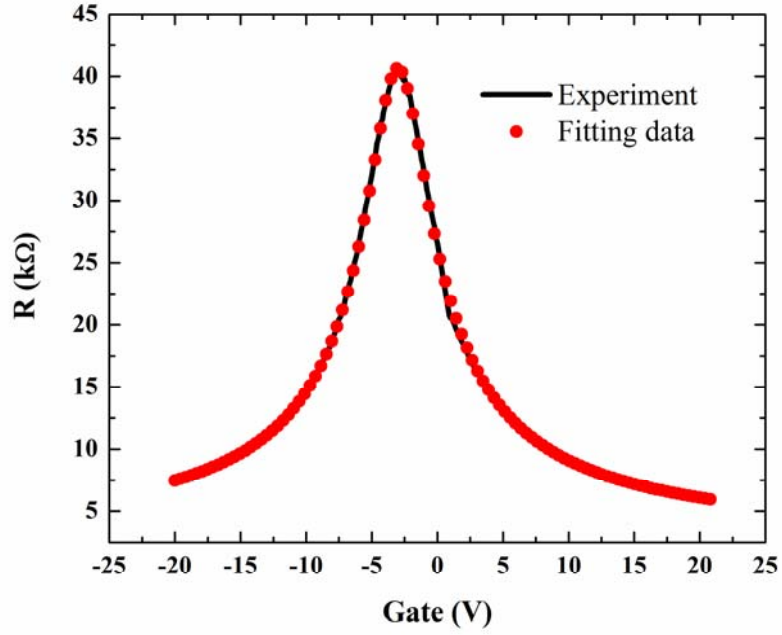


FIG. S3. Resistance measured as a function of gate voltage and relevant fitting.

IV. Bias voltage dependence

We have measured sample B1 at different bias voltages. The small bias data of sample B1 is shown below. Since there is a transport gap in the antidot graphene sample as shown in Fig. 1(c), transport at finite V_{sd} shows a strong nonlinear G - V_{sd} characteristic, and conductance is smaller at lower bias voltages. We have lowered the bias voltage to 10 mV, so that the corresponding power is lowered to a quarter of the power at 20 mV. The mesoscopic scaling behavior still exists and the value of the dephasing length still remains the same at 10 μm .

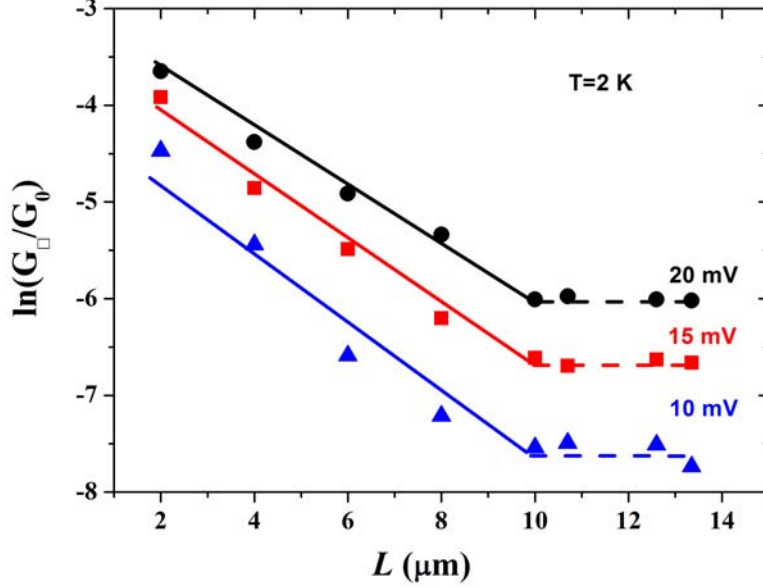


FIG. S4. Logarithm of G_{\square}/G_0 of sample B1 plotted as a function of sample size L at different bias voltage. The solid lines are linear fit to the conductance data of sample size smaller than $10 \mu\text{m}$.

V. Additional experimental data on different antidot size and spacing

We have performed additional experiments on two different samples—B1 and B2. They are both in the Hall bar geometry (as shown in Fig. 1(a)) but with different antidot size and spacing. The antidot diameter is 90 nm for B1 and 120 nm for B2. The periodicity still remains at 150 nm . The antidots are arranged in triangular lattice, just as sample set A.

At 2 K , the conductance of B1 and B2 at CNP is plotted as a function of L in Fig. S5. It is clearly seen that the most remarkable difference induced by the antidot size/spacing is the localization length.

The localization length of B1, which has a smaller antidot size (90 nm), and hence larger ribbon width, is $\xi=3.4 \mu\text{m}$ while the localization length of B2 with the larger antidot size (120 nm), and hence smaller ribbon width, is $\xi=1.12 \mu\text{m}$. This conforms with physical picture that the localization length is shorter when the constriction between dot is smaller so that the elastic mean free path is smaller.

The localization length can also be adjusted by applying a magnetic field. We have measured the localization length under different magnetic field by the same method

as before. For B1, $\xi(0.25 \text{ T})=4.4 \mu\text{m}$, $\xi(0.5 \text{ T})=5.7 \mu\text{m}$, $\xi(1 \text{ T})=9.1 \mu\text{m}$; for B2, $\xi(1 \text{ T})=1.5 \mu\text{m}$, $\xi(2 \text{ T})=2.0 \mu\text{m}$, $\xi(3 \text{ T})=2.6 \mu\text{m}$, $\xi(4 \text{ T})=3.0 \mu\text{m}$. We normalize the applied field by B_0 (B_0 for B1 is 0.04 T, for B2 is 0.13 T) and then plot them in Fig. R3(b). Excellent agreement is seen.

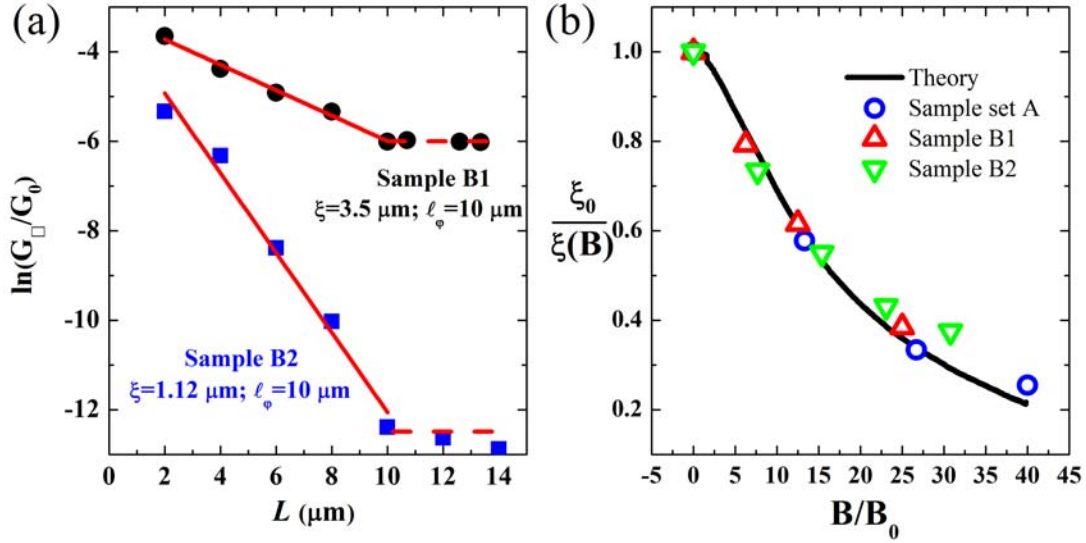


FIG. S5. (a) Logarithm of G_{\square}/G_0 at 2 K plotted as a function of sample size L of B1 and B2. (b) Inverse of localization length is plotted as a function of the magnetic field, normalized by B_0 . Here ξ_0 is the zero field value of the localization length.

We can use the same analysis as described in the main text to check how the scaling parameters change with the antidot size/spacing. For sample B1, using the equation $\xi \cong l_m \exp[(\pi/2)k_F l_m]$, a mean free path $l_m = 33 \text{ nm}$ is obtained. From $B_0 = 0.04 \text{ T}$, we have $B/B_0 = (ev_F^2 \tau^2 / \hbar) e^{1/\lambda} B$, in which B_0 is seen to be a function of the elastic scattering time τ , and $\lambda = \hbar / E_F \tau$ is a dimensionless coupling constant. This relation between B_0 and τ offers an alternative approach to estimate the elastic mean free path. We obtain $\tau = 32 \text{ fs}$, and the mean free path is $l_m = v_F \tau = 32 \text{ nm}$, which is in good agreement with the mean free path 33 nm obtained earlier. By the same analysis, for sample set B2, a mean free path 26 nm can be obtained from the localization length and 24 nm from the B_0 .

VI. Magnetic field dependence of ξ_{VRH} .

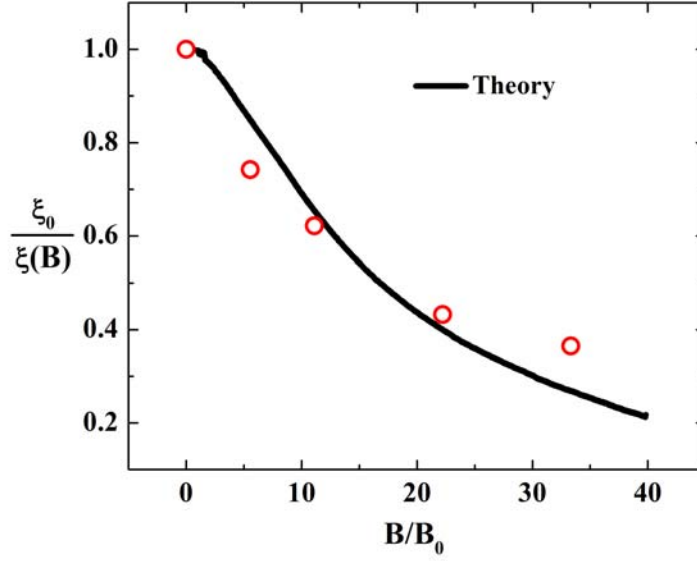


FIG. S6. Magnetic field dependence of ξ_{VRH} . Inverse of ξ_{VRH} is plotted as a function of the magnetic field, normalized by B_0 .

The hopping distance ξ_{VRH} , interpreted as the localization length of the VRH states, can also be increased by an applied magnetic field shown in Fig. S6. A value of $B_1 = 0.09$ T is obtained from the best fit, from which we deduce an elastic mean scattering time τ_m^{VRH} . The associated elastic mean free path is $l_m^{VRH} = v_F \tau_m^{VRH} = 26$ nm. However, from the relation $\xi_{VRH} \cong l_m^{VRH} \exp[(\pi/2)k_F l_m^{VRH}]$, we obtain $l_m^{VRH} \approx 11$ nm. This discrepancy may imply that the relation between ξ_{VRH} and l_m^{VRH} , valid in the limit of weak elastic scatterings, may be inapplicable to the present case.

References

- [1] B. I. Shklovskii, and A. L. Efros, *Electronic properties of doped semiconductors* (Springer-Verlag, Berlin, 1984).
- [2] C. Jang, S. Adam, J. H. Chen, E. D. Williams, S. Das Sarma, and M. S. Fuhrer, *Phys. Rev. Lett.* **101**, 146805 (2008).
- [3] A. Konar, T. Fang, and D. Jena, *Phys. Rev. B* **82**, 115452 (2010).